The Astrophysical Journal Supplement Series, 247:31 (9pp), 2020 March https://doi.org/10.3847/1538-4365/ab700e

A Comprehensive Catalog of Dark Matter Halo Models for SPARC Galaxies

Pengfei Li[1], Federico Lelli[2,3], Stacy McGaugh[1], and James Schombert[4]
[1] Department of Astronomy, Case Western Reserve University, Cleveland, OH 44106, USA; PengfeiLi0606@gmail.com, pxl283@case.edu
[2] European Southern Observatory, Karl-Schwarschild-Strasse 2, Garching bei München, Germany
[3] School of Physics and Astronomy, Cardiff University, Queens Buildings, The Parade, Cardiff, CF24 3AA, UK
[4] Department of Physics, University of Oregon, Eugene, OR 97403, USA
Received 2019 December 1; revised 2020 January 21; accepted 2020 January 24; published 2020 March 10

Abstract

We present rotation curve fits to 175 late-type galaxies from the *Spitzer* Photometry and Accurate Rotation Curves database using seven dark matter (DM) halo profiles: pseudo-isothermal, Burkert, Navarro–Frenk–White (NFW), Einasto, Di Cintio et al. (2014, hereafter DC14), cored-NFW, and a new semi-empirical profile named Lucky13. We marginalize over the stellar mass-to-light ratio, galaxy distance, disk inclination, halo concentration, and halo mass (and an additional shape parameter for Einasto) using a Markov Chain Monte Carlo method. We find that cored halo models, such as the DC14 and Burkert profiles, generally provide better fits to rotation curves than the cuspy NFW profile. The stellar mass-halo mass relation from abundance matching is recovered by all halo profiles once imposed as a Bayesian prior, whereas the halo mass–concentration relation is not reproduced in detail by any halo model. We provide an extensive set of figures as well as best-fit parameters in machine-readable tables to facilitate model comparison and the exploration of DM halo properties.

Unified Astronomy Thesaurus concepts: Galaxy dark matter halos (1880); Galaxy dynamics (591); Galaxy formation (595); Galaxy evolution (594); Galaxy rotation curves (619); Galaxy kinematics (602); Dark matter distribution (356); Cold dark matter (265); Spiral galaxies (1560); Dwarf galaxies (416); Late-type galaxies (907)

Supporting material: figure sets, machine-readable table

1. Introduction

Rotation curves reveal a discrepancy between dynamically determined and optically measured masses of galaxies (Rubin et al. 1978; Bosma 1981; van Albada et al. 1985). Together with other astrophysical evidences, this led to the introduction of dark matter. Since then, various dark matter (DM) halo profiles have been proposed, such as the pseudo-isothermal (pISO) and Navarro–Frenk–White (NFW; Navarro et al. 1996) profiles.

Lelli et al. (2016) built the *Spitzer* Photometry and Accurate Rotation Curves (SPARC) database, including 175 late-type galaxies with extended H I/Hα rotation curves and near-infrared surface photometry. This galaxy sample provides us the opportunity to make a comprehensive survey of halo models by fitting all the data in a homogeneous fashion.

A large amount of rotation curve fits can serve the purpose of exploring DM halo properties and potential correlations. For example, in Li et al. (2019), we fit two simulation-motivated profiles, the Einasto (Einasto 1965) and DC14 (Di Cintio et al. 2014) profiles, to the SPARC galaxies and find that the halo scale radius and surface density of the DM halo correlate with the galaxy luminosity with a similar power law, while the characteristic volume density is a constant. This finding benefits from the wide ranges in stellar masses, surface brightnesses, and gas fractions that the SPARC galaxies span.

In this paper, we provide rotation curve fits to 175 SPARC galaxies using seven halo models with/without ΛCDM motivated priors, depending on the availability of the priors for each profile. Summary tables and figures are organized by galaxy and by halo profile together with the best-fit parameters, so that readers can easily look up these fits for their own research. The results are made publicly available on the SPARC website.

2. Data, Models, and Method

2.1. The SPARC Sample

The SPARC database[5] (Lelli et al. 2016) includes 175 late-type galaxies with high-quality H I/Hα rotation curves and near-infrared *Spitzer* photometry. The H I measurements allow tracing the rotation velocity ($V_{\rm obs}$) out to large radii, providing strong constraints on the DM halo profiles. The *Spitzer* photometry has a key benefit: the stellar mass-to-light ratio has little scatter at 3.6 μm (e.g., McGaugh & Schombert 2014; Meidt et al. 2014; Schombert et al. 2019). This effectively helps in breaking the disk–halo degeneracy (van Albada et al. 1985) when delineating the contributions of the stellar disk and dark matter halo to the observed rotation curves. The mass models for the stellar disk and bulge (when present) are built by numerically solving the Poisson equation for the observed surface brightness profile at 3.6 μm. Similarly, the mass contribution of the gas is derived from the observed H I surface density profile, scaled up to include helium. The derived gravitational potentials of the baryonic components are represented by the circular velocities of test particles, tabulated as $V_{\rm disk}$, $V_{\rm bul}$, and $V_{\rm gas}$ corresponding to the contributions of the stellar disk, bulge, and gas, respectively. For convenience, the stellar contributions in the SPARC database are tabulated using a mass-to-light ratio of unity in solar units and need to be scaled down to more realistic values at 3.6 μm (Lelli et al. 2016; Starkman et al. 2018).

SPARC is a large sample by the standard of H I interferometry. It includes all late-type galaxies from spirals to dwarf irregulars and spans a large range of stellar masses (5 dex) and surface brightnesses (>3 dex). This makes the

[5] astroweb.case.edu/SPARC

SPARC sample ideal for model testing and exploring the properties of DM halos.

Galaxy distances in the SPARC database are measured via five different methods (see Lelli et al. 2016 for details): Hubble flow assuming $H_0 = 73$ km s^{-1} Mpc^{-1} and correcting for Virgo-centric infall, the tip magnitude of the red giant branch, the period–luminosity relation of Cepheids, membership to the Ursa major cluster of galaxies, and Type Ia supernovae. Disk inclinations are estimated kinematically. We treat distance and inclination as nuisance parameters, marginalizing over their uncertainty by imposing Gaussian priors with a standard deviation equal to their formal uncertainty.

2.2. Dark Matter Halo Profiles

In this paper, we attempt to investigate all available DM profiles, including pISO, Burkert, NFW, Einasto, DC14, cored-NFW, and a new semi-empirical profile that we call Lucky13. In general, each halo profile contains two fitting parameters: a scale radius, r_s, and a characteristic volume density, ρ_s. For convenience, the free parameters in our fits are the concentration, C_{200}, and the rotation velocity, V_{200}, which are defined as

$$C_{200} = r_{200}/r_s;\ V_{200} = 10\ C_{200} r_s H_0, \tag{1}$$

where r_{200} is the radius inside of which the average halo density is 200 times the critical density of the universe. For consistency, we use these cosmologically motivated definitions also for purely empirical DM profiles, such as the pISO and Burkert models. In the following section, we describe each halo model in detail.

pISO. Rotation curves of dwarf galaxies are found to be well fit by an empirical profile with a constant-density core, the pseudo-isothermal profile (see e.g., Adams et al. 2014; Oh et al. 2015), and

$$\rho_{\rm pISO} = \frac{\rho_s}{1 + \left(\frac{r}{r_s}\right)^2}. \tag{2}$$

The enclosed mass profile is given by

$$M_{\rm pISO} = 4\pi\rho_s r_s^3 [x - \arctan(x)], \tag{3}$$

where we have introduced the dimensionless parameter $x = r/r_s$. The corresponding rotation velocity profile is

$$\frac{V_{\rm pISO}}{V_{200}} = \sqrt{\frac{1 - \arctan(x)/x}{1 - \arctan(C_{200})/C_{200}}}. \tag{4}$$

Burkert. The enclosed mass of the pISO profile quickly diverges at large radii (Equation (3)). Burkert (1995) proposed a modified version of the pISO profile that diverges more slowly,

$$\rho_{\rm Burkert} = \frac{\rho_s}{\left(1 + \frac{r}{r_s}\right)\left[1 + \left(\frac{r}{r_s}\right)^2\right]}, \tag{5}$$

with an enclosed halo mass profile given by

$$M_{\rm Burkert} = 2\pi\rho_s r_s^3 \left[\frac{1}{2}\ln(1 + x^2) + \ln(1 + x) - \arctan(x)\right]. \tag{6}$$

Its rotation velocity is then given by

$$\frac{V_{\rm Burkert}}{V_{200}} = \sqrt{\frac{C_{200}}{x}} \times \sqrt{\frac{\frac{1}{2}\ln(1 + x^2) + \ln(1 + x) - \arctan(x)}{\frac{1}{2}\ln(1 + C_{200}^2) + \ln(1 + C_{200}) - \arctan(C_{200})}}. \tag{7}$$

NFW. *N*-body DM-only simulations of structure formation predict a cuspy profile (Navarro et al. 1996),

$$\rho_{\rm NFW} = \frac{\rho_s}{\left(\frac{r}{r_s}\right)\left[1 + \left(\frac{r}{r_s}\right)\right]^2}, \tag{8}$$

which goes as $\rho \propto r^{-1}$ at small radii and $\rho \propto r^{-3}$ at large radii. Its enclosed mass profile is

$$M_{\rm NFW} = 4\pi\rho_s r_s^3 \left[\ln(1 + x) - \frac{x}{1 + x}\right], \tag{9}$$

corresponding to the rotation velocity profile

$$\frac{V_{\rm NFW}}{V_{200}} = \sqrt{\frac{C_{200}}{x}\frac{\ln(1 + x) - x/(1 + x)}{\ln(1 + C_{200}) - C_{200}/(1 + C_{200})}}. \tag{10}$$

Einasto. Using high-resolution DM-only simulations, Navarro et al. (2004) find that the simulated halos can be better described by the Einasto profile (Einasto 1965),

$$\rho_{\rm Einasto} = \rho_s \exp\left\{-\frac{2}{\alpha_\epsilon}\left[\left(\frac{r}{r_s}\right)^{\alpha_\epsilon} - 1\right]\right\}, \tag{11}$$

which introduces an additional shape parameter, α_ϵ. When $\alpha_\epsilon > 0$, the profile has a finite central density. Its enclosed mass profile (Mamon & Łokas 2005; Merritt et al. 2006) is

$$M_{\rm Einasto} = 4\pi\rho_s r_s^3 \exp\left(\frac{2}{\alpha_\epsilon}\right)\left(\frac{2}{\alpha_\epsilon}\right)^{-\frac{3}{\alpha_\epsilon}} \times \frac{1}{\alpha_\epsilon}\Gamma\left(\frac{3}{\alpha_\epsilon}, \frac{2}{\alpha_\epsilon}x^{\alpha_\epsilon}\right), \tag{12}$$

where $\Gamma(a, x) = \int_0^x t^{a-1}e^{-t}dt$ is the incomplete Gamma function, and the velocity profile is given by

$$\frac{V_{\rm Einasto}}{V_{200}} = \sqrt{\frac{C_{200}}{x}\frac{\Gamma\left(\frac{3}{\alpha_\epsilon}, \frac{2}{\alpha_\epsilon}x^{\alpha_\epsilon}\right)}{\Gamma\left(\frac{3}{\alpha_\epsilon}, \frac{2}{\alpha_\epsilon}C_{200}^{\alpha_\epsilon}\right)}}. \tag{13}$$

The shape parameter α_ϵ depends on the halo mass (Dutton & Macciò 2014),

$$\alpha_\epsilon = 0.0095\nu^2 + 0.155, \tag{14}$$

where $\log\nu = -0.11 + 0.146m + 0.0138m^2 + 0.00123m^3$ and $m = \log(M_{\rm halo}/10^{12}h^{-1}M_\odot)$. Simulated DM halos present a standard deviation of 0.16 dex around the mean relation. However, in real galaxies, the final distribution of α_ϵ differs significantly from this relation if we do not impose it as a Bayesian prior (Li et al. 2019). We hence include this relation as part of the ΛCDM priors (explained in Section 2.3).

DC14. According to cosmological simulations of galaxy formation, baryonic matter accreted within the halos could

exert a feedback effect on the halo and hence modify its halo profiles. Di Cintio et al. (2014) consider the baryonic feedback due to supernovae using a set of zoomed-in, hydrodynamic simulations. They establish the DC14 model, whose profile is defined in terms of the model class (α, β, and γ; Hernquist 1990; Zhao 1996),

$$\rho_{\alpha\beta\gamma} = \frac{\rho_s}{\left(\frac{r}{r_s}\right)^{\gamma}\left[1+\left(\frac{r}{r_s}\right)^{\alpha}\right]^{(\beta-\gamma)/\alpha}}, \quad (15)$$

where β and γ are, respectively, the inner and outer slopes, and α describes the transition between the inner and outer regions. The values of these parameters depend on the stellar-to-halo mass ratio (SHM),

$$\begin{aligned}\alpha &= 2.94 - \log[(10^{X+2.33})^{-1.08} + (10^{X+2.33})^{2.29}],\\ \beta &= 4.23 + 1.34X + 0.26X^2,\\ \gamma &= -0.06 + \log[(10^{X+2.56})^{-0.68} + 10^{X+2.56}], \end{aligned} \quad (16)$$

where $X = \log(M_\star/M_{\rm halo})$ is the SHM ratio in logarithmic space. Its enclosed mass profile is given by

$$M_{\rm DC14} = 4\pi r_s^3 \rho_s \frac{1}{\alpha}[B(a, b+1, \epsilon) + B(a+1, b, \epsilon)], \quad (17)$$

where $B(a, b, x) = \int_0^x t^{a-1}(1-t)^{b-1}dt$ is the incomplete Beta function, and we define $a = (3-\gamma)/\alpha$, $b = (\beta-3)/\alpha$, and $\epsilon = \frac{(r/r_s)^\alpha}{1+(r/r_s)^\alpha}$. Thus, its velocity profile is given by

$$\frac{V_{\rm DC14}}{V_{200}} = \sqrt{\frac{C_{200}}{x}\frac{B(a, b+1, \epsilon) + B(a+1, b, \epsilon)}{B(a, b+1, \epsilon_c) + B(a+1, b, \epsilon_c)}}. \quad (18)$$

Equation (16) only works for the SHM ratio within $(-4.1, -1.3)$, since this is the range where the supernovae feedback is significant and dominant. At $X < -4.1$, the energy released by supernovae is insufficient to modify the initial cuspy profile so that an NFW profile remains. At $X > -1.3$, feedback due to active galactic nuclei might start to dominate. We hence set $X = -1.3$ as the largest acceptable value, following Katz et al. (2017).

The fitting results for the Einasto and DC14 profiles are presented in Li et al. (2019). For completeness and comparison, we also include those fits in this paper.

coreNFW. More recently, Read et al. (2016a, 2016b) investigate the evolution of isolated dwarf galaxies using high-resolution hydrodynamic simulations. They conclude that long-time evolution can transform an inner cusp into a finite central core through repeated bursts of star formation. They provide a general fitting function for the evolved DM profile in terms of the NFW profile,

$$M_{\rm coreNFW}(<r) = M_{\rm NFW}(<r) f^n, \quad (19)$$

where $f = \tanh\left(\frac{r}{r_c}\right)$ acts to cancel the central cusp. The core size r_c is proportional to the stellar half-mass–radius $R_{1/2}$ and $r_c = \eta\, R_{1/2}$, where the proportional constant η is suggested to be 1.75. There could be some galaxy-to-galaxy scatter around this value of η, but we keep it fixed to minimize the number of free parameters in the fit.

How shallow the core becomes is controlled by the evolution parameter n ($0 < n < 1$). When $n = 1$, it is a complete core, while $n = 0$ corresponds to a cusp. Therefore, the evolution of the halo profile is traced by the value of n, which is given by

$$n = \tanh\left(\kappa \frac{t_{\rm SF}}{t_{\rm dyn}}\right), \quad (20)$$

where the so-called star formation time, $t_{\rm SF}$, is set to 14 Gyr since all SPARC galaxies are at $z = 0$, the tuning parameter κ is set to 0.04 as suggested by the simulations of Read et al. (2016a), and the dynamic time, $t_{\rm dyn}$, is defined as

$$t_{\rm dyn} = 2\pi\sqrt{\frac{r_s^3}{GM_{\rm NFW}(r_s)}}. \quad (21)$$

For the SPARC galaxies, this gives values of n spanning the range 0.1–1.0. The resulting cored-NFW (coreNFW) profile has a volume density profile given by

$$\rho_{\rm coreNFW} = f^n \rho_{\rm NFW} + \frac{n f^{n-1}(1-f^2)}{4\pi r^2 r_c} M_{\rm NFW}. \quad (22)$$

Lucky13. We construct another cored profile from the (α, β, and γ) models by considering the specific case of $\gamma = 0$ to reach a finite core and $\beta = 3$ to get the same decreasing rate as the NFW profile at large radii. The transition parameter is simply set as $\alpha = 1$. This gives us the following profile,

$$\rho_{130} = \frac{\rho_s}{\left[1+\left(\frac{r}{r_s}\right)\right]^3}, \quad (23)$$

which we call Lucky13. Its enclosed mass profile is given by

$$M_{130} = 4\pi\rho_s r_s^3\left[\ln(1+x) + \frac{2}{1+x} - \frac{1}{2(1+x)^2} - \frac{3}{2}\right], \quad (24)$$

corresponding to the velocity profile

$$\frac{V_{130}}{V_{200}} = \sqrt{\frac{C_{200}}{x}\frac{\ln(1+x) + \frac{2}{1+x} - \frac{1}{2(1+x)^2} - \frac{3}{2}}{\ln(1+C_{200}) + \frac{2}{1+C_{200}} - \frac{1}{2(1+C_{200})^2} - \frac{3}{2}}}. \quad (25)$$

2.3. MCMC Simulations

We fit the observed rotation velocities by summing the contribution of each component,

$$V_{\rm tot}^2 = V_{\rm DM}^2 + \Upsilon_{\rm disk} V_{\rm disk}^2 + \Upsilon_{\rm bul} V_{\rm bul}^2 + V_{\rm gas}^2. \quad (26)$$

In general, DM profiles have two free parameters: V_{200} and C_{200} (the Einasto profile has an additional shape parameter, α_ϵ). For the baryonic contributions, there are also three adjustable parameters: the stellar mass-to-light ratio, $\Upsilon_\star$; the galaxy distance, D; and the disk inclination, i. They comprise a five- (six for Einasto) dimensional parameter space. To fit these halo profiles, we map the posterior distributions of these fitting parameters using the open python package *emcee* (Foreman-Mackey et al. 2013). As in Li et al. (2019), we impose lognormal priors on $\Upsilon_\star$ around their fiducial values ($\Upsilon_{\rm disk} = 0.5$ and $\Upsilon_{\rm bul} = 0.7$ according to McGaugh et al. 2016; Lelli et al. 2017) with a standard deviation of 0.1 dex suggested by stellar population synthesis models (e.g., see Bell & de Jong 2001; Portinari et al. 2004; Meidt et al. 2014;

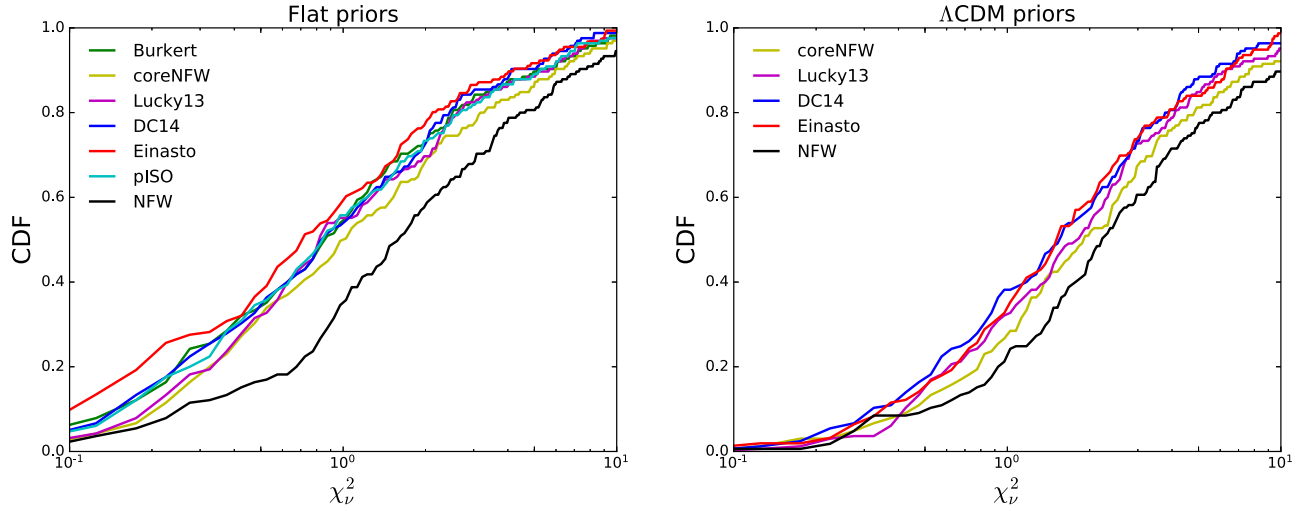

Figure 1. Cumulative distributions of the reduced χ^2_ν for seven halo profiles with flat (left) and ΛCDM priors (right).

Schombert et al. 2019) and Gaussian priors on D and i around their mean values as tabulated in the SPARC database with standard deviations given by their uncertainties.

As for halo parameters, we set general loose boundaries for them: $10 < V_{200} < 500$ km s^{-1} and $0 < C_{200} < 1000$. Within these ranges, flat priors are imposed for all considered halo profiles. For the NFW, Einasto, DC14, coreNFW, and Lucky13 profiles, we also impose the ΛCDM priors, which are comprised of the SHM relation (Moster et al. 2013) and the halo mass–concentration relation (Macciò et al. 2008). The multi-epoch abundance matching determines the relation between stellar and DM halo masses,

$$\frac{M_\star}{M_{200}} = 2N\left[\left(\frac{M_{200}}{M_1}\right)^{-\beta} + \left(\frac{M_{200}}{M_1}\right)^{\gamma}\right]^{-1}, \tag{27}$$

where $\log(M_1) = 11.59$, $N = 0.0351$, $\beta = 1.376$ and $\gamma = 0.608$. Moster et al. (2013) estimated the scatter to be $\sigma(\log M_\star) = 0.15$ dex around this relation. This prior, together with the lognormal prior on stellar mass-to-light ratios, robustly breaks the disk–halo degeneracy.

Macciò et al. (2008) show that the concentration and halo mass are correlated via a power law,

$$\log(C_{200}) = a - b\log(M_{200}/[10^{12}h^{-1}M_\odot]), \tag{28}$$

where the coefficients a and b depend on cosmology and halo profile. For the NFW, coreNFW, and Lucky13 profiles, we use the values from the *5 year Wilkinson Microwave Anisotropy Probe* (*WMAP5*) cosmology corresponding to $H_0 = 72$ km s^{-1} Mpc^{-1}, which is close to the value adopted for the SPARC database:

$$a = 0.830, \quad b = -0.098. \tag{29}$$

Di Cintio et al. (2014) show that the concentration for the DC14 profile is related to that of NFW by

$$C_{200,\mathrm{DC14}} = C_{200,\mathrm{NFW}}(1.0 + e^{0.0001[3.4(X+4.5)]}). \tag{30}$$

For the Einasto profile, the coefficients as shown in Li et al. (2019) are

$$a = 0.977, \quad b = -0.130. \tag{31}$$

Equation (28) is the mean concentration–halo mass relation, and it has an intrinsic scatter of 0.11 dex.

We choose the likelihood function as $\exp\left(-\frac{1}{2}\chi^2\right)$, where χ^2 is defined as

$$\chi^2 = \sum_R \frac{[V_{\mathrm{obs}}(R) - V_{\mathrm{tot}}(R)]^2}{(\delta V_{\mathrm{obs}})^2}, \tag{32}$$

where V_{obs} is the observed rotation velocity and δV_{obs} is the observational uncertainty. The final posterior probability is proportional to the product of the likelihood function and priors according to Bayes theorem.

We use the standard affine-invariant ensemble sampler in *emcee* as in Li et al. (2019). We initialize the Markov Chain Monte Carlo (MCMC) chains with 200 random walkers and the size of stretch-move $a = 2$. We run 500 iterations for the burn-in period and then reset the sampler before running another 2000 iterations. We check that the acceptance fractions for most galaxies are within 10% and 70%. There are a few galaxies with lower acceptance fractions, but their posterior distributions are well behaved. The parameter sets corresponding to the maximum probability are marked as the best-fit parameters. We estimate their uncertainties using the "std" output of GetDist,[6] which is an open Python package for analyzing Monte Carlo samples.

3. Results

In Figure 1, we plot the cumulative distribution function of the reduced χ^2 $\left(\chi^2_\nu = \frac{\chi^2}{N-f}\right)$ for all the halo profiles. Among these profiles, the Einasto profile with flat priors on halo parameters has the best-fit quality since it has the largest number of fitting parameters. In general, cored profiles, such as Burkert, coreNFW, DC14, Einasto, and pISO, provide better rotation curve fits than the cuspy NFW profile, no matter if we impose ΛCDM priors (the combination of the stellar-to-halo mass relation and halo mass–concentration relation, as well as Equation (14) for the Einasto profile) or not. When imposing the ΛCDM priors, the fit quality decreases for all halo profiles, but the adherence to ΛCDM scaling relations drastically improves, as we now discuss.

[6] https://getdist.readthedocs.io

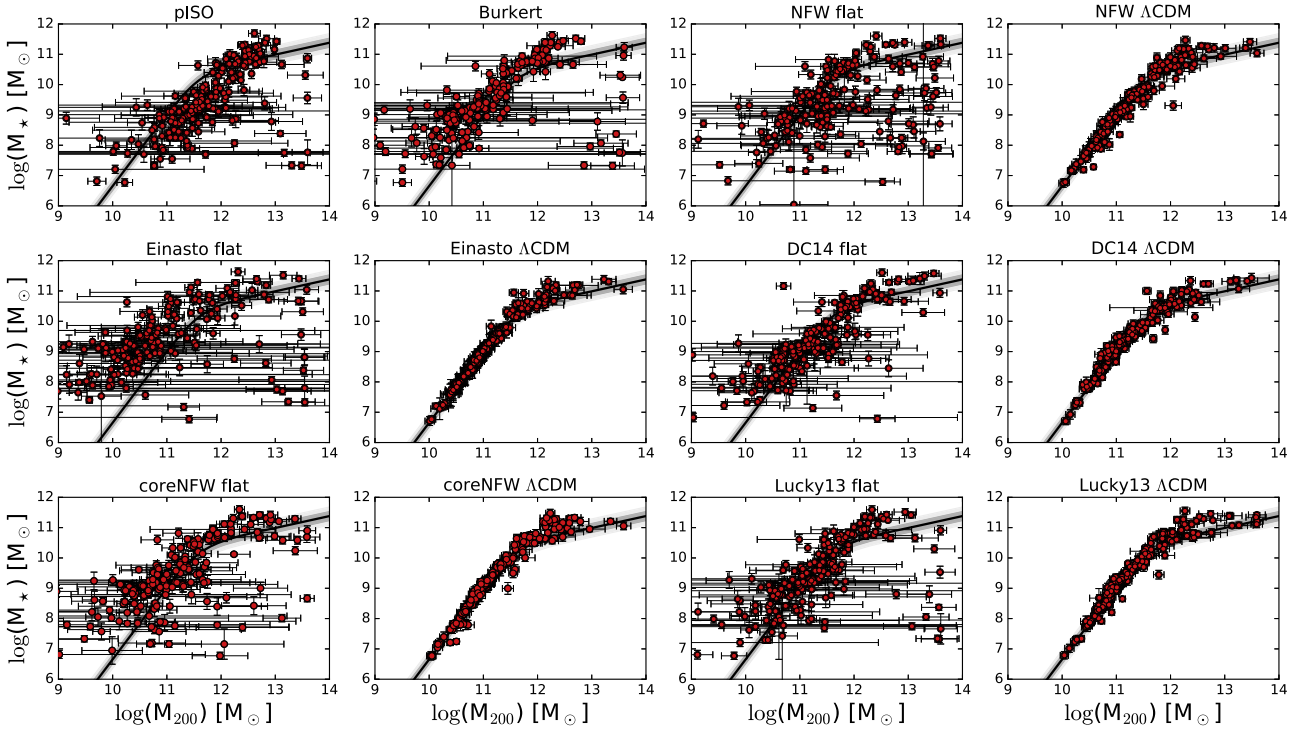

Figure 2. Relations between stellar masses and DM halo masses for the seven halo models. Solid lines show the expected stellar-halo mass relation (Moster et al. 2013), which is roughly recovered when the ΛCDM priors are imposed. Dark and light shadow regions correspond to 1σ and 2σ standard deviations, respectively.

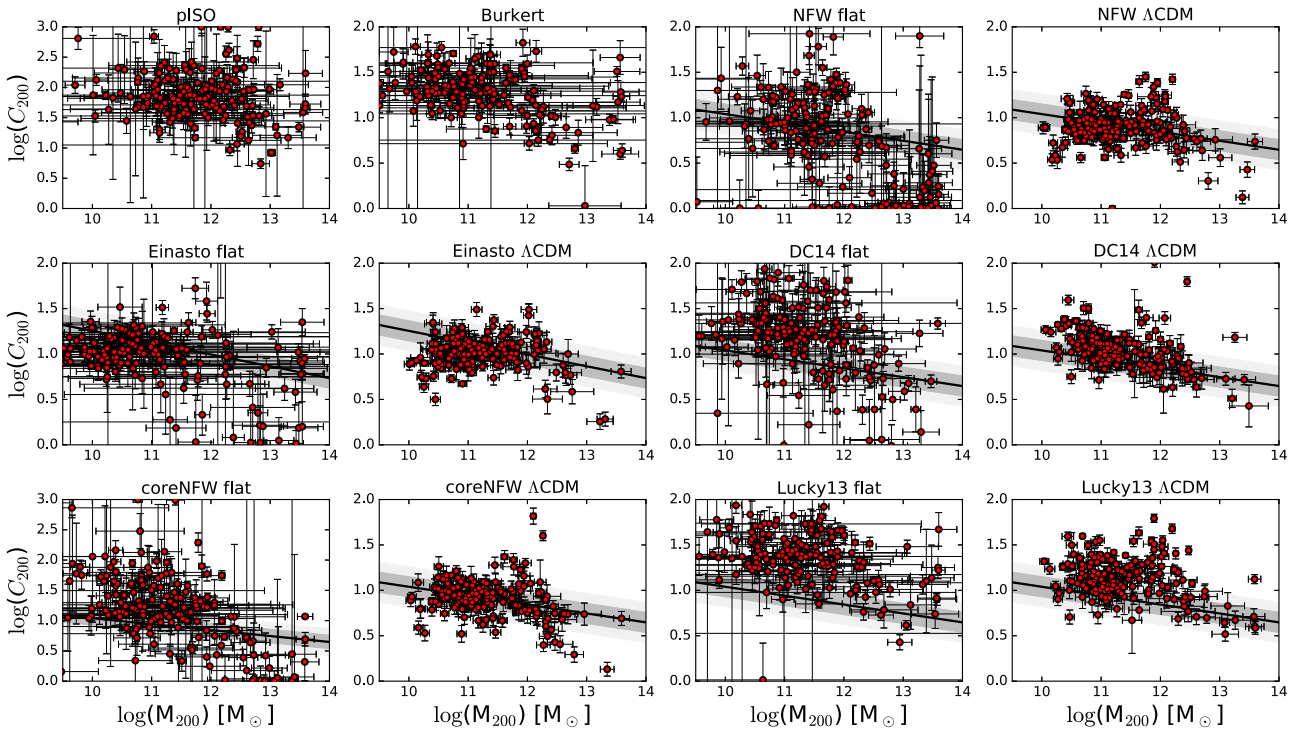

Figure 3. Concentrations of the SPARC galaxies against halo masses for the seven halo models. Solid lines are the expected relations from *N*-body simulations (Macciò et al. 2008), which are model dependent and not available for the pISO and Burkert profiles. Dark and light shadow regions represent 1σ and 2σ standard deviations, respectively. The concentrations for the DC14 profile have been converted to that for NFW in order to compare with the imposed relation.

We plot stellar versus halo masses in Figure 2. The stellar mass shows a positive correlation with the halo mass for all the halo models. When imposing flat priors, the DC14 profile presents the closest match to the SHM relation, with the smallest standard deviation of 1.01 dex. The Lucky13 profile also shows a relation that matches the expected SHM relation well except for a few outliers, resulting in a standard deviation of 1.24 dex. On the other hand, the Einasto, NFW, and coreNFW profiles display a much larger scatter, with standard deviations of 1.68 dex, 1.61 dex, and 1.36 dex,

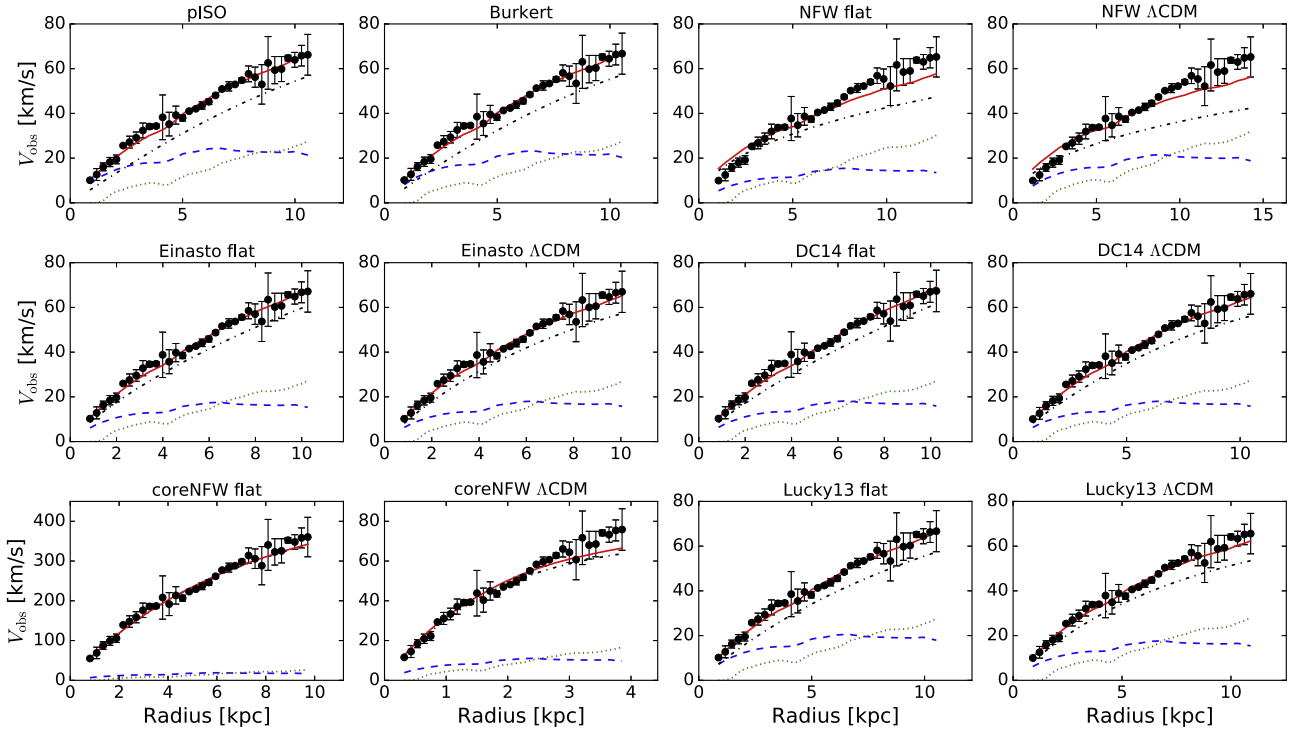

Figure 4. Example galaxy: the best-fit rotation curves of the dwarf galaxy IC 2574 using eight models with/without ΛCDM priors. Blue, green, purple, and black lines represent disk, gas, bulge (if present), and dark matter contributions, respectively. Solid red lines are the total rotation curves, and the shadow regions reflect 1σ (dark) and 2σ (light) confidence levels.

(The complete figure set (175 images) is available.)

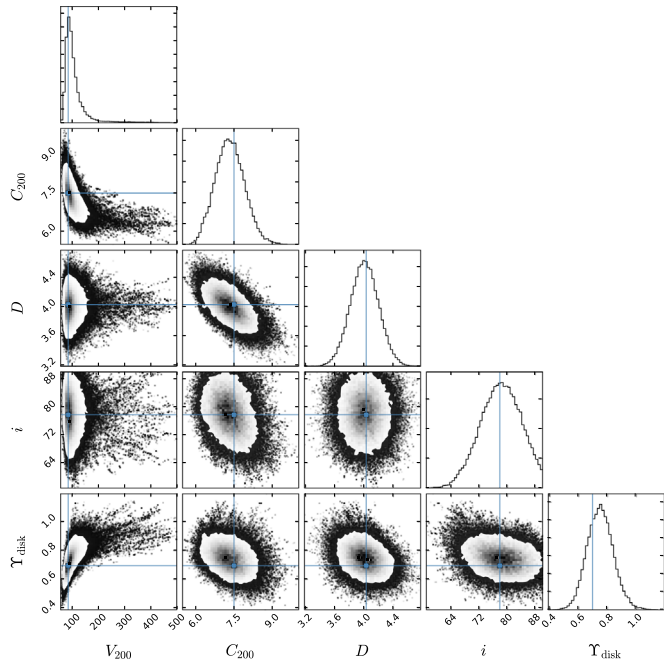

Figure 5. Posterior distributions of the fitting parameters for the example galaxy IC 2574 using the Burkert profile. The complete figure set for 175 SPARC galaxies using all the models (175 × 12 images) is available in the SPARC website. Also available are the corresponding Monte Carlo samples in the format required by the open Python package GetDist.

respectively. Finally, the Burkert and pISO profiles show mean vertical shifts of 0.51 and −0.44 dex with respect to the expected SHM relation, giving systematically higher and lower stellar masses.

When we impose the ΛCDM priors, the expected SHM relation is well reproduced at low halo masses for all halo profiles. For massive galaxies, the DM halo masses are mostly smaller than the abundance-matching prediction. The extent to which this deviation is significant depends on halo models: the DC14 profile provides the best agreement, while the NFW, coreNFW, and Lucky13 profiles show larger discrepancies. The disagreement at high halo masses for the NFW profile has been pointed out by Posti et al. (2019), who argued for a linear SHM relation for late-type galaxies. They imposed the mass–concentration relation as a prior but did not impose the SHM relation. We here confirm that there exist some discrepancies at high halo masses for the NFW profile even when we impose the SHM relation as a prior (see also Katz et al. 2017).

We plot halo concentration against the halo mass in Figure 3. When imposing flat priors, the pISO, Einasto, and Lucky13 profiles do not present clear trends between concentrations and halo masses, with Spearman's correlation coefficients between −0.1 and −0.3. The Burkert, NFW, DC14, and coreNFW profiles show marginal evidence for anticorrelations, with Spearman's coefficients between −0.3 and −0.5. Moreover, these putative anticorrelations seem steeper than expected from cosmology. The halo mass–concentration relation is not as well recovered as the SHM relation even if it is imposed as part of the ΛCDM priors. Remarkably, in such a case, the DC14 model is the only one to present a significant anticorrelation (Spearman's coefficient of −0.5), but the relation appears systematically shifted toward higher concentrations. The other profiles (NFW, Einasto, coreNFW, and Lucky13) have Spearman's coefficients between 0.0 and −0.2 that are indicative of no correlations, as evinced by the relatively flat distributions of concentrations versus halo masses.

Table 1
The Best-fit Parameters for Galaxy IC 2574

Name	$\Upsilon_{\rm disk}$ ($M_\odot/L_\odot$)	$\Upsilon_{\rm bul}$ ($M_\odot/L_\odot$)	Distance (Mpc)	Inclination (deg.)	V_{200} (km s^{-1})	C_{200}	r_s (kpc)	$\log\rho_s$ ($M_\odot$ pc^{-3})	$\log(M_{200})$ ($M_\odot$)	α	χ^2_ν
pISO-Flat	0.77 ± 0.09	⋯	4.04 ± 0.20	80.0 ± 5.5	119.39 ± 57.47	14.76 ± 1.32	11.08 ± 5.43	−2.62 ± 0.90	11.73 ± 0.63	0.00 ± 0.00	2.51
Burkert-Flat	0.69 ± 0.09	⋯	4.03 ± 0.19	77.8 ± 5.6	85.83 ± 44.24	7.49 ± 0.57	15.69 ± 8.17	−2.52 ± 0.96	11.30 ± 0.67	0.00 ± 0.00	2.41
NFW-Flat	0.26 ± 0.05	⋯	4.83 ± 0.19	87.4 ± 2.1	105.03 ± 5.57	1.00 ± 0.01	143.87 ± 7.74	−4.29 ± 0.10	11.57 ± 0.07	0.00 ± 0.00	36.55
NFW-LCDM	0.44 ± 0.05	⋯	5.45 ± 0.16	88.4 ± 1.8	78.56 ± 2.99	1.00 ± 0.01	107.59 ± 4.36	−4.29 ± 0.07	11.19 ± 0.05	0.00 ± 0.00	36.30
Einasto-Flat	0.41 ± 0.10	⋯	3.92 ± 0.20	76.2 ± 6.4	275.92 ± 98.58	1.64 ± 0.81	230.07 ± 140.20	−4.49 ± 0.95	12.83 ± 0.47	0.33 ± 0.10	36.30
Einasto-LCDM	0.44 ± 0.09	⋯	3.84 ± 0.20	76.8 ± 5.9	63.18 ± 3.50	4.71 ± 0.25	18.39 ± 1.42	−3.33 ± 0.13	10.90 ± 0.07	0.76 ± 0.06	36.30
DC14-Flat	0.44 ± 0.10	⋯	3.92 ± 0.20	75.4 ± 6.4	123.50 ± 11.53	7.68 ± 0.79	22.03 ± 3.05	−2.83 ± 0.18	11.78 ± 0.12	0.00 ± 0.00	2.17
DC14-LCDM	0.42 ± 0.05	⋯	4.00 ± 0.19	80.8 ± 4.8	67.56 ± 3.12	9.53 ± 0.59	9.72 ± 0.75	−2.68 ± 0.10	10.99 ± 0.06	0.00 ± 0.00	2.43
coreNFW-Flat	0.50 ± 0.12	⋯	3.71 ± 0.20	10.4 ± 0.9	495.74 ± 49.16	11.69 ± 0.62	58.11 ± 6.54	−2.01 ± 0.20	13.59 ± 0.13	0.00 ± 0.00	3.08
coreNFW-LCDM	0.43 ± 0.09	⋯	1.47 ± 0.20	59.3 ± 8.8	54.70 ± 4.82	14.65 ± 0.80	5.12 ± 0.53	−1.77 ± 0.18	10.72 ± 0.11	0.00 ± 0.00	6.22
Lucky13-Flat	0.54 ± 0.11	⋯	4.02 ± 0.20	77.9 ± 5.7	105.99 ± 32.05	7.09 ± 0.73	20.49 ± 6.54	−2.37 ± 0.57	11.58 ± 0.39	0.00 ± 0.00	2.27
Lucky13-LCDM	0.39 ± 0.06	⋯	4.17 ± 0.19	83.7 ± 3.9	74.04 ± 3.07	7.99 ± 0.47	12.70 ± 0.92	−2.26 ± 0.11	11.11 ± 0.05	0.00 ± 0.00	2.70

Note. The complete table for all 175 galaxies is available in the SPARC website.

(This table is available in its entirety in machine-readable form.)

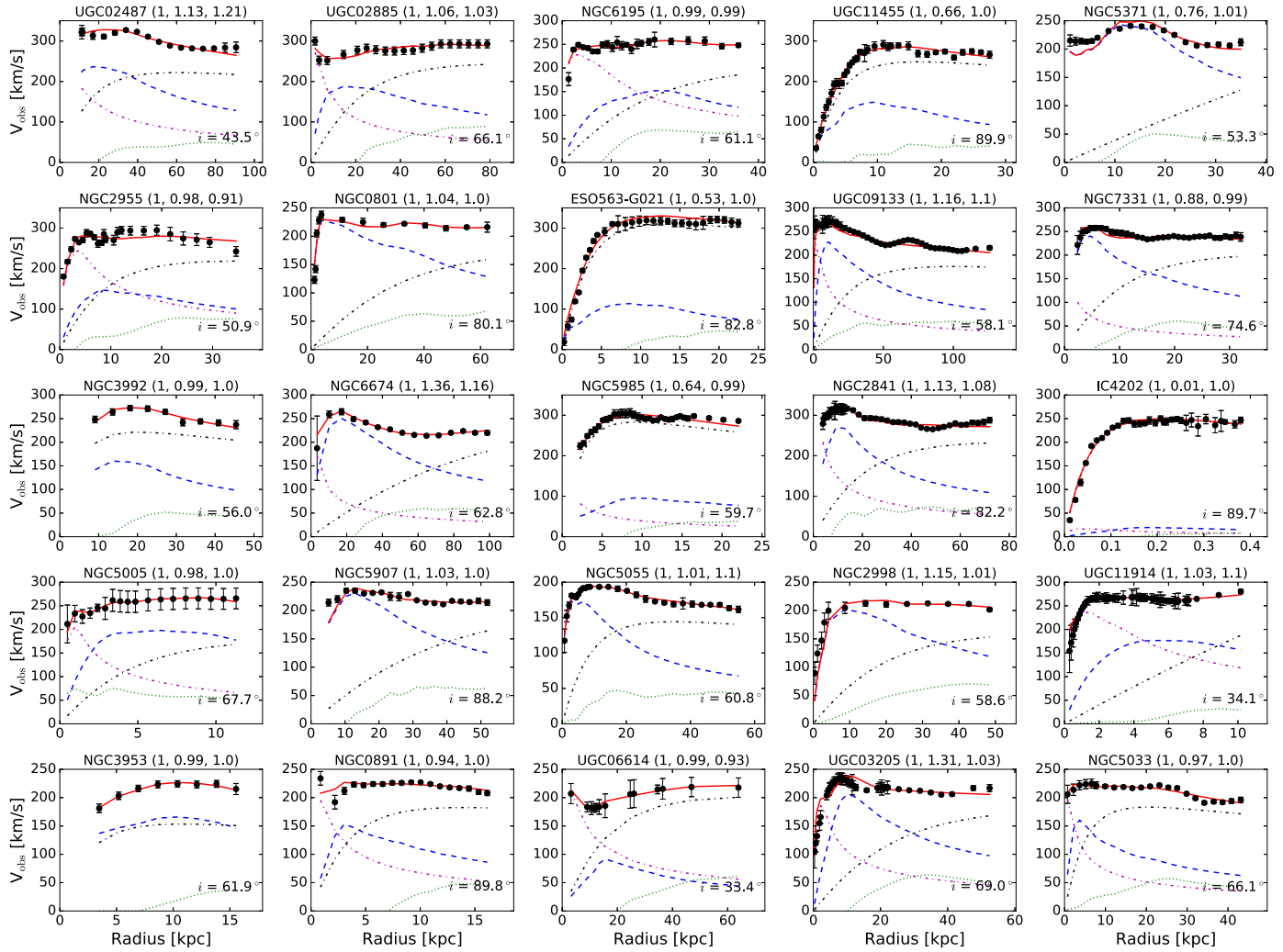

Figure 6. Example model: the best rotation curve fits of 175 SPARC galaxies using the Burkert profile. Lines are the same as those in Figure 4. The three numbers in the parentheses of the subtitles are the quality flag Q (for details see Lelli et al. 2016) and the ratios of the best-fit distances and inclinations to their original values, respectively. Best-fit inclination is shown within each panel. Galaxies are ordered by decreasing quality and luminosity. The complete figure set for all the halo models (7×12 images) is available.

(The complete figure set (84 images) is available.)

In Figure, 4 we show the fits for an example galaxy, IC 2574, using all the models. We list the best-fit parameters in Table 1. Its posterior distribution using the Berkurt profile is shown in Figure 5 as an example. In Figure 6, we show the fits of all SPARC galaxies using the Burkert profile. Similar figures and tables are available on the SPARC website for all 175 galaxies and all seven halo profiles.

4. Conclusion

In this paper, we provide the community with a homogeneous catalog of DM halo parameters for 175 galaxies from the SPARC database, considering seven different halo models. Homogeneity is an important guarantee for fair comparisons of models, as Korsaga et al. (2019) find that different fitting procedures can lead to significantly different fitting results. The halo parameters are derived by performing MCMC fits to H I/Hα rotation curves. We impose flat priors on the halo parameters, Gaussian priors on the galaxy distance and disk inclination, and lognormal prior on the stellar mass-to-light ratio. For five DM halo models, we also present rotation curve fits, imposing basic ΛCDM priors: the stellar mass-halo mass relation from abundance matching and the mass–concentration relation from cosmological simulations. In general, cored DM profiles provide better fits than the cuspy NFW. Moreover, while the stellar mass-halo mass relation is generally recovered by all halo models when imposed as a prior, the mass–concentration relation is not reproduced in detail by any halo model. All the fit results are publicly available on the SPARC database in the form of machine-readable tables and summary figures.

This work was supported in part by NASA ADAP grant 80NSSC19k0570.

ORCID iDs

Pengfei Li https://orcid.org/0000-0002-6707-2581
Federico Lelli https://orcid.org/0000-0002-9024-9883
Stacy McGaugh https://orcid.org/0000-0002-9762-0980
James Schombert https://orcid.org/0000-0003-2022-1911

References

Adams, J. J., Simon, J. D., Fabricius, M. H., et al. 2014, ApJ, 789, 63
Bell, E. F., & de Jong, R. S. 2001, ApJ, 550, 212
Bosma, A. 1981, AJ, 86, 1825
Burkert, A. 1995, ApJL, 447, L25
Di Cintio, A., Brook, C. B., Dutton, A. A., et al. 2014, MNRAS, 441, 2986
Dutton, A. A., & Macciò, A. V. 2014, MNRAS, 441, 3359
Einasto, J. 1965, TrAlm, 5, 87
Foreman-Mackey, D., Hogg, D. W., Lang, D., & Goodman, J. 2013, PASP, 125, 306
Hernquist, L. 1990, ApJ, 356, 359
Katz, H., Lelli, F., McGaugh, S. S., et al. 2017, MNRAS, 466, 1648
Korsaga, M., Epinat, B., Amram, P., et al. 2019, MNRAS, 490, 2977
Lelli, F., McGaugh, S. S., & Schombert, J. M. 2016, AJ, 152, 157
Lelli, F., McGaugh, S. S., Schombert, J. M., & Pawlowski, M. S. 2017, ApJ, 836, 152
Li, P., Lelli, F., McGaugh, S. S., Starkman, N., & Schombert, J. M. 2019, MNRAS, 482, 5106
Macciò, A. V., Dutton, A. A., & van den Bosch, F. C. 2008, MNRAS, 391, 1940
Mamon, G. A., & Łokas, E. L. 2005, MNRAS, 362, 95
McGaugh, S. S., Lelli, F., & Schombert, J. M. 2016, PhRvL, 117, 201101
McGaugh, S. S., & Schombert, J. M. 2014, AJ, 148, 77
Meidt, S. E., Schinnerer, E., van de Ven, G., et al. 2014, ApJ, 788, 144
Merritt, D., Graham, A. W., Moore, B., Diemand, J., & Terzić, B. 2006, AJ, 132, 2685
Moster, B. P., Naab, T., & White, S. D. M. 2013, MNRAS, 428, 3121
Navarro, J. F., Frenk, C. S., & White, S. D. M. 1996, ApJ, 462, 563
Navarro, J. F., Hayashi, E., Power, C., et al. 2004, MNRAS, 349, 1039
Oh, S.-H., Hunter, D. A., Brinks, E., et al. 2015, AJ, 149, 180
Portinari, L., Sommer-Larsen, J., & Tantalo, R. 2004, MNRAS, 347, 691
Posti, L., Fraternali, F., & Marasco, A. 2019, A&A, 626, A56
Read, J. I., Agertz, O., & Collins, M. L. M. 2016a, MNRAS, 459, 2573
Read, J. I., Iorio, G., Agertz, O., & Fraternali, F. 2016b, MNRAS, 462, 3628
Rubin, V. C., Ford, W. K., Jr., & Thonnard, N. 1978, ApJL, 225, L107
Schombert, J., McGaugh, S., & Lelli, F. 2019, MNRAS, 483, 1496
Starkman, N., Lelli, F., McGaugh, S., & Schombert, J. 2018, MNRAS, 480, 2292
van Albada, T. S., Bahcall, J. N., Begeman, K., & Sancisi, R. 1985, ApJ, 295, 305
Zhao, H. 1996, MNRAS, 278, 488